

# Neural Canonical Transformation for the Spectra of Fluxional Molecule $\text{CH}_5^+$

Ruiqi Wang,<sup>1,2</sup> Qi Zhang,<sup>1,\*</sup> and Lei Wang<sup>1,†</sup>

<sup>1</sup>Beijing National Laboratory for Condensed Matter Physics and Institute of Physics, Chinese Academy of Sciences, Beijing 100190, China

<sup>2</sup>School of Physical Sciences, University of Chinese Academy of Sciences, Beijing 100190, China

(Dated: September 30, 2025)

Protonated methane,  $\text{CH}_5^+$ , is a highly fluxional molecule with large spatial motions of the hydrogen atoms. The molecule's anharmonic effects and the scrambling of the hydrogen atoms significantly affect the excitation spectrum of the molecule. The neural canonical transformation (NCT) approach, which we previously developed to solve the vibrational spectra of molecules and solids, is a powerful method that effectively treats nuclear quantum effects and anharmonicities. Using NCT with wavefunctions in atomic coordinates rather than normal coordinates, we successfully calculate the ground and excited states of  $\text{CH}_5^+$ . We found that the wavefunctions for the ground state, as well as for low- and high-energy excited states, show preferences for the three stationary points on the potential energy surface. Furthermore, the dynamics of all these states are characterized by continuous hydrogen swapping. This work extends the applicability of the NCT approach for calculating excited states to fluxional molecules without fixed geometry.

## I. INTRODUCTION

Protonated methane,  $\text{CH}_5^+$ , is known for its highly fluxional nature with rapid scrambling dynamics of the five protons [1–4]. It represents the prototypic superacid that plays a pivotal role as a reactive intermediate in acid-catalyzed electrophilic reactions [5, 6], and is also considered a crucial intermediate in the formation of polyatomic organic compounds within cold interstellar clouds [7, 8]. Although initially observed by mass spectroscopy in the early 1950s [9], the first infrared (IR) spectrum of  $\text{CH}_5^+$  was not successfully measured until 1999 [10], yet it remained unassigned. Another breakthrough occurred in 2015 with the measurement of experimental combination differences by Asvany et al. [11] (with an improvement reported in Ref. [12]), serving as another key experiment in advancing the understanding of  $\text{CH}_5^+$  [13]. The combination difference is the difference of two transition wavenumbers that share a common energy level. Subtracting them cancels the shared level and retrieves the energy spacing of the other two levels.

Concurrent with experimental progress, significant advancements in numerical methods have emerged. An ab initio calculation of the millimeter-wave spectrum of  $\text{CH}_5^+$  [14] and an MP2/cc-pVTZ-based potential energy surface (PES) [15] were reported in 2003. In 2004, diffusion Monte Carlo (DMC) techniques are applied to the ground state calculation of  $\text{CH}_5^+$  with an ab initio based PES [16–18]. Then in 2006, a full-dimensional PES based on CCSD(T)/aug-cc-pVTZ data that could successfully capture the dissociation process of  $\text{CH}_5^+$  was reported [19], becoming the state-of-the-art PES of  $\text{CH}_5^+$  since then. Subsequently, researchers have applied various methods to investigate the (ro-)vibrational excited states and the infrared spectrum of  $\text{CH}_5^+$  and its isotopologs. These include large-scale vibrational configuration interaction (VCI) calculations [20, 21], DMC methods [22–24], contracted basis-iterative method [25–28], (multilayer)

multiconfigurational time-dependent Hartree method [29], the molecule superrotor model method [30, 31], and the quantum-graph (QG) model [32–35]. Despite significant advances in experimental and computational methods, the accurate assignment of spectral lines for  $\text{CH}_5^+$  remains an unsolved problem. Consequently, considerable effort is still required to interpret its spectrum and elucidate the molecule's complex dynamics.

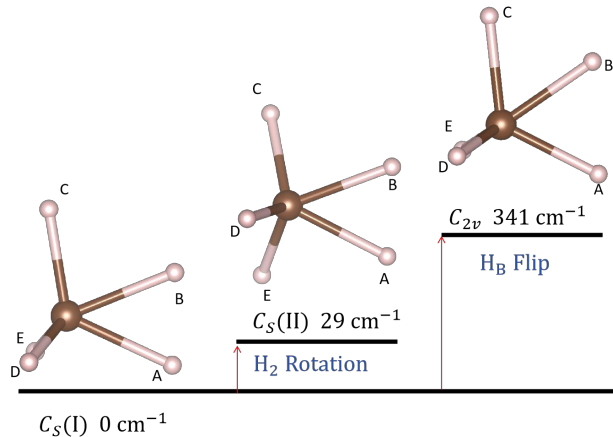


Figure 1. The structures of the three stationary points on the  $\text{CH}_5^+$  PES with energies relative to the global minimum at the CCSD(T) level from Ref. [21]. In the  $C_s$ (I) configuration, the hydrogens A, B, and C lie in the same plane as the central carbon. D and E are positioned symmetrically with respect to this plane. The  $\text{H}_2$  moiety is formed by A and B. In the  $C_s$ (II) configuration, the  $\text{H}_2$  moiety (also formed by A and B) is rotated by  $30^\circ$  relative to the  $C_s$ (I) configuration, and another  $30^\circ$  rotation of the  $\text{H}_2$  moiety would lead back to another  $C_s$ (I) configuration. In the  $C_{2v}$  configuration, the hydrogens labeled A and C are symmetric with respect to the plane formed by D, B, E, and the central carbon.

The addition of a proton to methane ( $\text{CH}_4$ ) to form  $\text{CH}_5^+$  causes a significant structural deviation from the tetrahedral geometry of methane. The relatively rigid structure of  $\text{CH}_4$  creates high energy barriers that prevent the free permutation

\* zhangqi94@iphy.ac.cn

† wanglei@iphy.ac.cn

of its hydrogen atoms during molecular vibration. This allows each hydrogen atom to be uniquely labeled. An equilibrium geometry with an arbitrary but fixed numbering of the atoms can be chosen as a reference configuration. During vibration, the molecule primarily explores regions of the PES near this reference geometry [36, 37]. Because the dynamics are localized in this manner, analyses based on normal coordinates are both appropriate and successful [38–40]. In contrast, the PES of  $\text{CH}_5^+$  features 120 equivalent minima that differ from one another only by the permutation of hydrogen atoms. These minima are interconnected by low-energy barriers, which permit hydrogen exchange even in the quantum ground state and cause the ground-state wavefunction to be delocalized over all 120 configurations. Adjacent minima on the PES are connected by stationary points of different symmetries. Starting from a global minimum with  $C_s(\text{I})$  symmetry, a  $C_s(\text{II})$  stationary point is accessed via a  $30^\circ$  rotation of the  $\text{H}_2$  moiety. Alternatively, a flip motion that exchanges hydrogens between the  $\text{H}_2$  and the  $\text{CH}_3$  components proceeds through a  $C_{2v}$  stationary point (see Fig. 1, visualized by VESTA [41]). Both stationary points represent low energy barriers relative to the global minimum: the barrier height is only  $29 \text{ cm}^{-1}$  for the  $C_s(\text{II})$  point and  $341 \text{ cm}^{-1}$  for the  $C_{2v}$  point. The resulting fluxionality of  $\text{CH}_5^+$  produces a complex energy level structure across its spectrum. A prime example is the  $175 \text{ cm}^{-1}$  level, which is assigned to a highly anharmonic  $\text{H}_\text{B}$  flip isomerization [21]—a large-amplitude motion with no counterpart in the spectrum of rigid  $\text{CH}_4$ . Furthermore, approximately 900 spectral lines are observed in the  $2770\text{--}3150 \text{ cm}^{-1}$  region, as reported in Ref. [10], which significantly exceeds the number of spectral lines found in that region for  $\text{CH}_4$  and  $\text{CH}_3^+$  [42].

The application of machine learning methods to the computation of the PES and (ro-)vibrational energy levels has recently gained significant attention as an emerging trend [43–53]. Among these methods, the neural canonical transformation (NCT) [43] is a notable variational approach for the scalable and simultaneous computation of multiple excited states. The method begins with an initial set of orthogonal basis functions and employs a neural network to transform this basis into the optimum wavefunctions. This transformation is designed to strictly preserve orthogonality. A key advantage of NCT is that it provides direct access to the wavefunctions, which simplifies the calculation of physical properties. The NCT approach has been successfully applied to various systems, including the thermal properties of interacting fermions [54], the effective mass of interacting electrons [55], the equation of state of dense hydrogen in extreme situations [56], the quantum anharmonic effects of quantum solids [57], the vibrational eigenstates of molecules [43] and the high-pressure water ice [58].

The primary objective of this paper is to apply the NCT method to compute the ground and excited eigenstates of the highly fluxional molecule  $\text{CH}_5^+$ . Our previous implementation of NCT [43] used normal coordinates, which are defined with respect to a single molecular reference configuration. This approach is unsuitable for a highly fluxional system like  $\text{CH}_5^+$ , whose wavefunction is delocalized over many equivalent configurations [25]. A calculation based on

a single reference geometry will fail to capture the wavefunction’s amplitude in configurations corresponding to hydrogen exchange. Therefore, extending the NCT method to accurately model such fluxional molecules is of significant interest. To address this challenge, we present an NCT implementation that operates directly on the three-dimensional Cartesian coordinates of the atoms. This approach is independent of any reference configuration and is harnessed here to compute the eigenstates of  $\text{CH}_5^+$ . The code is available at <https://github.com/Callo42/nct-protonated-methane>.

## II. METHODS

This section is organized as follows. First, we set up the nuclear Schrödinger equation. Second, we detail the NCT technique, covering the basis set, the construction of the target wavefunctions, the energy estimation procedure, and the optimization of the wavefunction ansatz. Finally, we compare the NCT method with other computational approaches for  $\text{CH}_5^+$  calculations.

### A. Hamiltonian

In this work, we investigate the ground and excited states of  $\text{CH}_5^+$  by solving the time-independent Schrödinger equation for the nuclear Hamiltonian. Under the Born-Oppenheimer approximation, the potential energy of the molecule is given by a function of its nuclear coordinates  $\mathbf{x}$ . Under these considerations, the Hamiltonian reads:

$$H = - \sum_{i,\alpha} \frac{1}{2m_i} \frac{\partial^2}{\partial x_{i\alpha}^2} + V(\mathbf{x}), \quad (1)$$

where  $m_i$  is the mass of the  $i$ -th atom and  $\alpha$  is summed over three spatial dimensions. We use the ab initio-based, full-dimensional PES  $V(\mathbf{x})$  that is fitted to 36,173 CCSD(T)/aug-cc-pVTZ calculations from Ref. [19]. As pointed out in Ref. [26], starting from normal coordinates is not sufficient for an accurate calculation of  $\text{CH}_5^+$ . Therefore, we switch the coordinate system from the normal coordinates in our previous work [43] to the three-dimensional Cartesian coordinates.

### B. Neural Canonical Transformation

In this study, we employ a normalizing flow [59, 60] model to realize the NCT. This method performs a unitary transformation on an initial basis to yield wavefunctions that incorporate physical interactions, such as anharmonic effects [55]. Consider the one-dimensional toy problem illustrated in Fig. 2. We begin with an orthonormal basis set composed of one-dimensional Hermite functions,  $\{\Phi_n\}$ , where  $n$  is the excitation number and each function is an eigenstate of a one-dimensional harmonic oscillator (HO). A neural network then parameterizes a bijective mapping from this simple basis to the set of true, anharmonic wavefunctions,  $\{\Psi_n\}$ .

This transformation is constructed to preserve orthonormality while simultaneously introducing anharmonic effects into the final wavefunctions.

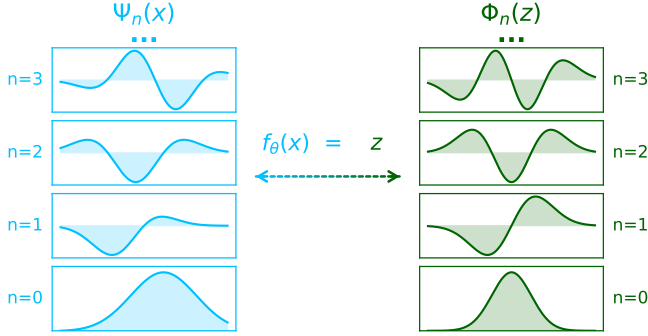


Figure 2. Neural Canonical Transformation: a sketch on a one-dimensional example. The  $\Psi_n(x)$  in the left panel denotes the true wavefunction and the  $\Phi_n(f_\theta(x))$  on the right refers to the wavefunction basis.  $f_\theta(x)$  in the middle is the bijection parameterized by neural network that connects two sets of wavefunctions.

The NCT method employed in this work uses a framework similar to our previous study [43]. However, to properly describe the fluxional nature of  $\text{CH}_5^+$ , we use Cartesian coordinates. The first step in calculating the eigenstates of the Hamiltonian in Eq. (1) is to define the wavefunction basis,  $\{\Phi_n(z)\}$ , in a latent space. This basis is constructed as the Hartree product of 18 one-dimensional HO wavefunctions:

$$\Phi_n(z) = \prod_{i=1}^{18} \phi_{n_i}(z_i), \quad (2)$$

where

$$\phi_{n_i}(z_i) = \frac{1}{\sqrt{2^{n_i} n_i!}} \left( \frac{m_i \omega_i}{\pi} \right)^{1/4} e^{-\frac{m_i \omega_i z_i^2}{2}} H_{n_i} \left( \sqrt{m_i \omega_i} z_i \right), \quad (3)$$

here  $\mathbf{n} = (n_1, n_2, \dots, n_{18})$  is the vector of quantum numbers, and  $\mathbf{z} = (z_1, z_2, \dots, z_{18})$  represents the coordinates in the 18-dimensional latent space. Each dimension  $i$  is associated with a mass  $m_i$  and a harmonic frequency  $\omega_i$ . For our  $\text{CH}_5^+$  calculation, the first three coordinates are assigned the mass of a carbon atom, while the remaining 15 are assigned the mass of a hydrogen atom. All calculations are performed in atomic units, with final results converted to other units, such as wavenumbers, where appropriate.

To prevent the use of a reference configuration that could hinder ergodicity to the molecule's 120 equivalent minima, each one-dimensional Hermite function is initialized around the origin. The frequencies are set to treat identical atoms equally: the 15 oscillators corresponding to the hydrogen atoms are assigned a single frequency,  $\omega_H$ , and the three oscillators for the carbon atom are assigned a different frequency,  $\omega_C$ , where  $\omega_C < \omega_H$ . This construction defines our 18-dimensional wavefunction basis in the latent space. The quantum number of each basis function  $\mathbf{n}$  is ordered as follows: we first denote  $n = 0$  as the ground state, and fix the carbon coordinates to be  $(0, 0, 0)$ . Then we order the indices

by sorting the basis energy  $E_{\text{HO}} = \sum_{i=4}^{18} n_i \omega_i$  in ascending order and truncate at a specific energy. Note that here we omit the zero-point energy  $\frac{1}{2} \sum_{i=4}^{18} \omega_i$  in  $E_{\text{HO}}$ .

Then a NCT is established to transform the wavefunction basis  $\{\Phi_n(z)\}$  into the configuration space  $\mathbf{x}$ :

$$\Psi_n(\mathbf{x}) = \Phi_n(f_\theta(\mathbf{x})) \left| \det \left( \frac{\partial f_\theta(\mathbf{x})}{\partial \mathbf{x}} \right) \right|^{1/2}, \quad (4)$$

and the transformed wavefunctions  $\{\Psi_n(\mathbf{x})\}$  span a variational subspace of the Hamiltonian [61]. During the transformation, it is expected that interactions such as collective dynamics of the atoms or anharmonicity are introduced into the wavefunction. Here, we parameterize  $f_\theta(\mathbf{x})$  using real-valued non-volume-preserving (RNVP) transformations [43, 62]. For conciseness, we abbreviate  $\theta$  in the transformed wavefunction. The square root of the Jacobian determinant term,  $\left| \det \left( \frac{\partial f_\theta(\mathbf{x})}{\partial \mathbf{x}} \right) \right|^{1/2}$ , is introduced by the variable substitution process in normalizing flow and is the key factor that ensures the orthonormality of the transformed wavefunctions [43]:

$$\langle \Psi_n | \Psi_{n'} \rangle = \delta_{nn'}. \quad (5)$$

Then we estimate the energy levels of the Hamiltonian in Eq. (1) as:

$$E_{\mathbf{n}} = \langle \Psi_{\mathbf{n}} | H | \Psi_{\mathbf{n}} \rangle = \mathbb{E}_{\mathbf{x} \sim |\Psi_{\mathbf{n}}(\mathbf{x})|^2} [E_{\mathbf{n}}^{\text{loc}}(\mathbf{x})], \quad (6)$$

here,  $\mathbb{E}[\cdot]$  denotes the expectation of the quantity inside the square brackets. The term  $\langle \Psi_{\mathbf{n}} | H | \Psi_{\mathbf{n}} \rangle$  is the expectation value of the Hamiltonian for the eigenstate  $\Psi_{\mathbf{n}}$ . Finally,  $E_{\mathbf{n}}^{\text{loc}}(\mathbf{x})$  denotes the local energy of the wavefunction [43]:

$$E_{\mathbf{n}}^{\text{loc}}(\mathbf{x}) = \sum_{i,\alpha} -\frac{1}{2m_i} \left[ \frac{\partial^2}{\partial x_{i\alpha}^2} \ln |\Psi_{\mathbf{n}}(\mathbf{x})| + \left( \frac{\partial}{\partial x_{i\alpha}} \ln |\Psi_{\mathbf{n}}(\mathbf{x})| \right)^2 \right] + V(\mathbf{x}). \quad (7)$$

With access to the wavefunctions in Eq. (4), the energies in Eq. (6) are estimated by Markov chain Monte Carlo [63] sampling of the wavefunction. The summation of all the energy eigenvalues of the transformed wavefunctions,  $\sum_{\{\mathbf{n}\}} E_{\mathbf{n}}$ , constitutes the variational upper bound to the true energy summation, and minimizing this summation gives us the optimal variational estimation of the true wavefunctions [43, 61]. According to this principle, we find the optimal parameters  $\theta$  by setting the loss function in the training process as follow and minimize it:

$$\mathcal{L} = \sum_{\{\mathbf{n}\}} E_{\mathbf{n}}. \quad (8)$$

Here, the summation iterates over all the eigenstates in the transformed wavefunctions,  $\{\Psi_{\mathbf{n}}(\mathbf{x})\}$ . In practice, we can simultaneously solve for dozens or hundreds of energy levels, and consequently, this summation typically involves a similar number of terms.

The gradient of the loss function with respect to the neural network parameters is estimated as [43, 54, 55]:

$$\nabla_{\theta} \mathcal{L} = 2 \sum_{\{\mathbf{n}\}} \mathbb{E}_{\mathbf{x} \sim |\Psi_{\mathbf{n}}(\mathbf{x})|^2} [E_{\mathbf{n}}^{\text{loc}}(\mathbf{x}) \nabla_{\theta} \ln |\Psi_{\mathbf{n}}(\mathbf{x})|]. \quad (9)$$

We use the Adam [64] optimizer to perform gradient descent on the parameters. First, we pretrain the network for 100 steps toward one of the manually chosen  $C_{2v}$  configurations using maximum likelihood estimation. Then, we launch the NCT training process. The pretraining process offers a good initialization of the network parameters and improves the numerical stability of variational optimization. After convergence is reached, each energy level is measured following Eq. (6).

### C. Comparison to Other Methods

The theoretical methods for  $\text{CH}_5^+$  that have been discussed in Sec. I are certainly valuable approaches that have had success in different areas. However, they do still encounter various challenges. For instance, methods like VCI and iterative eigensolvers tend to need large basis sets for convergence, which can make scaling up the calculations to more excited states quite challenging. The superrotor and QG models, on the other hand, introduce several approximations to the PES, and combining different PES into the model can require considerable effort. DMC methods require manually constructing nodal surfaces under the fixed-node approximation, a process that depends on prior knowledge of the specific energy level. This dependence poses challenges for simultaneously computing multiple excited states, which is particularly important in the case of  $\text{CH}_5^+$ . Compared to existing computational methods for the spectra of  $\text{CH}_5^+$ , the NCT method stands out as an ab initio approach that readily and systematically scales to a large number of excited states and is able to seamlessly incorporate various PES.

## III. RESULTS

This section is organized as follows. We begin in Sec. III A by describing the numerical details of our calculations. In Sec. III B, we analyze the zero-point energy and radial distribution functions of the ground state. Next, Sec. III C presents the Lorentzian spectrum derived from the computed energy levels. Finally, Secs. III D and III E report our findings on relative similarity and hydrogen permutation worldlines for various states.

### A. Numerical Details

In this work, we carried out two calculations: the first involves a single calculation of the ground state, while the second focuses on obtaining the lowest 136 eigenstates of the  $\text{CH}_5^+$  nuclear Hamiltonian. All calculations were performed in atomic units for a system of one carbon and five hydrogen atoms (see Sec. II B). The RNVP [43, 62] network is initialized with 327,624 learnable parameters to ensure expressivity. The Adam [64] optimizer is set with an initial learning rate of  $10^{-4}$ . For the ground-state calculation we use a total batch size of 2400 for steady convergence behavior. For excitation calculations, we train our model with 100 batches per energy level

(136,000 in total), and we optimize for 56,000 iterations. The calculation took about 54 hours to complete on a single V100 GPU with 6 cores of Intel Xeon Gold 6230 CPUs. For energy estimation of the ground state, we make an extra 200 iterations of Monte Carlo (MC) sampling of the converged wavefunctions, resulting in the equivalent of 480,000 samples. The zero-point energy is directly estimated on the sampled wavefunction. For excited states, we make an extra 1,000 iterations of Monte Carlo sampling (the equivalent of 100,000 samples for each state) of the converged wavefunctions, and all the eigenstates we possessed in training are sampled simultaneously. For inspecting the radial distribution functions of C-H and H-H distances, the relative similarity to three stationary points and the worldline of each state in Sec. III, we use the final converged checkpoint and sample each wavefunction individually.

### B. Zero-point Energy and Radial Distribution Functions of Ground State

The zero-point energy we obtain is  $10977.89(0.03)$   $\text{cm}^{-1}$ , around  $60 \text{ cm}^{-1}$  above the quantum DMC result reported in Ref. [21]. The RNVP network used to construct the NCT does not intrinsically enforce the permutational symmetry of the five hydrogen atoms. Consequently, the calculated ground-state wavefunction is not strictly constrained to the correct  $A_1^+$  symmetry, which may contribute to the observed variational error. However, our initial basis is constructed from atomic coordinates centered at the origin with same hydrogen frequencies and is therefore symmetric with respect to hydrogen permutation. The RNVP network is thus the only component that can introduce a slight symmetry breaking. Despite this limitation, we will illustrate later that the NCT method successfully learns a delocalized wavefunction that explores all 120 equivalent minima on the PES, accurately capturing the fluxional nature of  $\text{CH}_5^+$ .

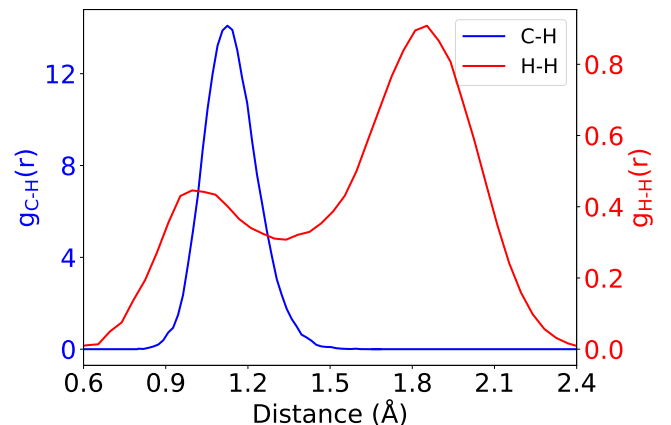


Figure 3. The radial distribution functions for C-H distances (in angstroms, left axis) and H-H distances (in angstrom, right axis) of the converged NCT wavefunction of ground state  $\text{CH}_5^+$ .

The radial distribution functions of C-H distances and H-

H distances of the ground state are shown in Fig. 3. The units of the C-H distances and the H-H distances are given in angstroms. As we initialize the hydrogen wavefunction as the Hartree product of identical one-dimensional HO wavefunctions, it is expected that the initial wavefunction would have five protons equally distributed on the sphere centered on the carbon atom. The structure of the  $\text{CH}_5^+$  is learned by the wavefunction as the NCT method explores the PES.

The results show that the C-H distances form a wide unimodal distribution. This indicates that all the C-H bonds have significant flexibility in length and it would be impossible to distinguish them from the bond length. The H-H distances form a bimodal distribution. The first peak occurs around 1.0 Å with weak intensity, and the main peak takes place around 1.9 Å. The 1.0 Å peak indicates that there are a significant number of hydrogen atoms that are close to each other, forming the  $\text{H}_2$  moiety. The 1.9 Å peak is formed by other hydrogen pairs. The unimodal C-H distances and bimodal H-H distances confirm that the quantum ground state is dominated by  $\text{CH}_3^+$  and  $\text{H}_2$ , which is also consistent with previous studies in Ref. [2, 18, 23].

### C. Excited States and Lorentzian Spectrum

The full excited energy levels of  $\text{CH}_5^+$  are listed in Table S1, in which the zero point energy is omitted and all the excited states are reported as relative energy differences to the zero point energy in  $\text{cm}^{-1}$ . Besides, we also calculate the lowest 24 excited energy levels of  $\text{CH}_4$  using the NCT method with the PES from Ref. [37] under normal coordinates, following the same scheme in Ref. [43].

In contrast to the IR spectrum reported in Ref. [21], which includes broadening from IR intensities, our approach generates a spectrum by directly broadening the calculated energy levels with equal weight for each level. To achieve this, we apply a Lorentzian convolution with a full-width-half-maximum (FWHM) of 30  $\text{cm}^{-1}$  to both our calculated NCT energy levels and the levels from harmonic approximations, as shown in Fig. 4. The harmonic approximation results for  $\text{CH}_5^+$  are from the normal mode frequencies in Ref. [19] and only contains fundamental levels above 900  $\text{cm}^{-1}$  due to the highly anharmonic feature of the low-frequencies levels [21]. The harmonic results for  $\text{CH}_4$  are from the harmonic approximation of the PES in Ref. [37].

In comparison to the harmonic approximations of  $\text{CH}_5^+$  and the NCT result of  $\text{CH}_4$ , the Lorentzian spectrum of  $\text{CH}_5^+$  displays notable discrepancies in several frequency regions. At low frequencies, a distinct set of levels near 100  $\text{cm}^{-1}$  is observed exclusively in the NCT spectrum of  $\text{CH}_5^+$ . These levels arise from strong anharmonicity and are generally absent in experimental spectra due to limited sensitivity in this domain, as demonstrated by the laser-induced reaction spectrum of Ref. [4]. No corresponding states are present in the more rigid  $\text{CH}_4$  molecule. Near 2000  $\text{cm}^{-1}$ ,  $\text{CH}_5^+$  has additional energy levels in a region forbidden by the harmonic approximation. The DMC method can also identify states within this region, provided the nodal surface is chosen properly. For ex-

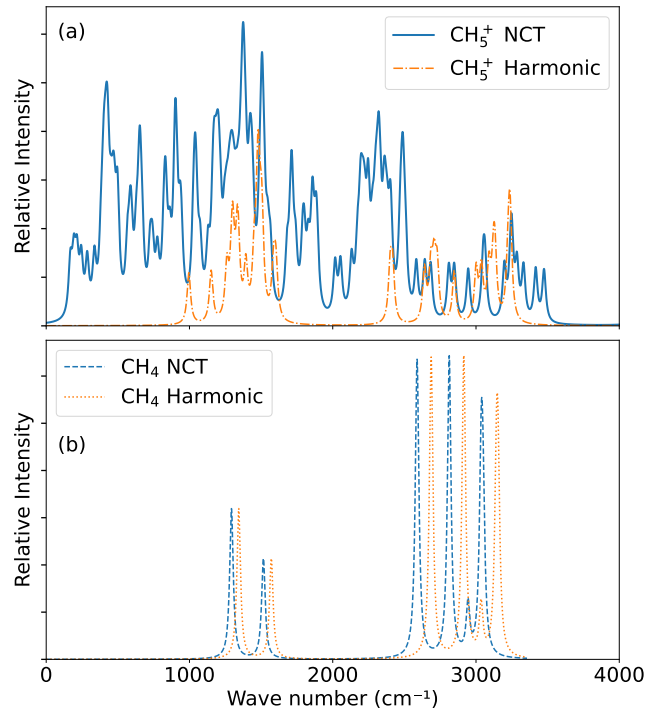


Figure 4. The Lorentzian spectra of the energy levels (convolved with FWHM of 30  $\text{cm}^{-1}$ ) for (a)  $\text{CH}_5^+$  and (b)  $\text{CH}_4$  from the NCT calculation and their harmonic approximations. The harmonic approximation result of  $\text{CH}_5^+$  is from the normal mode frequencies in Ref. [19]. The harmonic results of  $\text{CH}_4$  is from the PES we use from Ref. [37].

ample, Ref. [24] reports a high-symmetry state at 2164  $\text{cm}^{-1}$  found by DMC. However, due to the symmetry, such a state is generally forbidden or exhibits only negligible intensity in the IR spectrum. At higher frequencies, around 3000  $\text{cm}^{-1}$ ,  $\text{CH}_5^+$  displays a comparatively continuous spectral profile, whereas  $\text{CH}_4$  retains a discrete band structure.

In the  $\text{CH}_4$  molecule, atomic vibrations are confined near the equilibrium configuration. This gives rise to sharp and isolated spectral peaks for each normal mode. The NCT results primarily manifest as red shifts of the harmonic energy levels, in agreement with the findings of Ref. [37]. In contrast, due to the large anharmonicity, the spectrum of  $\text{CH}_5^+$  differs markedly from its harmonic approximation and is broadened across the spectrum, revealed by the NCT method. We will illustrate later that for both the low-energy and high-energy excited states, the molecule is experiencing large-amplitude spatial motion as well as hydrogen atom scrambling.

### D. Relative Similarity to three Stationary Points

For each chosen state, we first sample the converged wavefunction to generate 100,000 samples. From these samples, we calculate the root mean square deviation (RMSD) with respect to each of the three stationary points. We then take the reciprocals of these RMSD values and, finally, normal-

ize them to measure the relative similarity of each state to the stationary points, as illustrated in Fig. 5. For illustration, we choose the ground state and different excited states with energy levels of  $168.5\text{cm}^{-1}$ ,  $2016.5\text{cm}^{-1}$  and  $3049.9\text{cm}^{-1}$ .

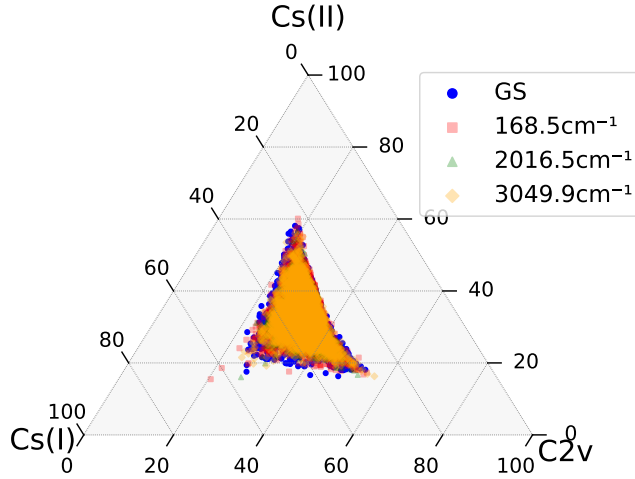


Figure 5. Ternary diagram of the relative similarity of samples from each state to the three types of stationary point configurations on PES. The values are percentages and are normalized for each sample.

The ground-state and excited-state distributions exhibit a common feature: both are centered and form three peaks directed toward the stationary points. This structure indicates a balanced preference for the  $C_s(I)$ ,  $C_s(II)$  and  $C_{2v}$  stationary points. Because the molecule in these states has a similar preference for each configuration, there is a significant probability of finding it in any of them. This probability signifies a delocalized wavefunction, which in turn facilitates hydrogen scrambling and allows the molecule to move among these three configurations.

### E. Hydrogen Worldline

We then focus on one of the walkers in the MC sampling process of the wavefunction for the ground state, the  $168.5\text{cm}^{-1}$ ,  $2016.5\text{cm}^{-1}$  and  $3049.9\text{cm}^{-1}$  state. They are extensively sampled for 1,000,000 steps and the hydrogen atom permutations are counted. The permutations are illustrated as a worldline in Fig. 6.

First, we choose one of the 120 equivalent global-minimum configuration, and label each hydrogen atom from A to E, as illustrated in Fig. 1. This specific configuration is chosen as the reference configuration. Then we choose one walker that has just been initialized for the MC sampling, label each hydrogen atom for this walker from A to E as well. As MC sampling proceeds the label of each hydrogen atom of the walker is fixed to the atom. Then at each step, we compare the snapshot of the current frame with the reference configuration, and find the permutation of the five hydrogen atoms such that, after the permutation, the sum of the pairwise distances of the hydrogen atoms with the same label is minimized. Then

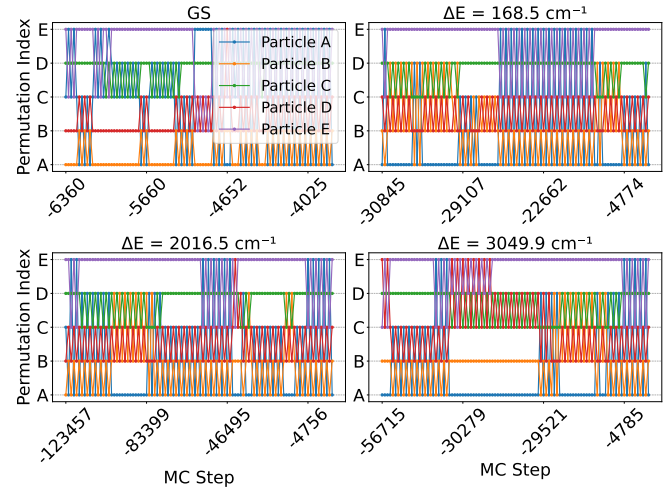


Figure 6. The H-atom permutation worldlines for the GS(ground state) and the  $168.5\text{cm}^{-1}$ ,  $2016.5\text{cm}^{-1}$  and  $3049.9\text{cm}^{-1}$  excited states. For each state we perform 1,000,000 MC sampling steps of the wavefunction and plot the last 100 permutations of H atoms. The permutation index is the manually chosen index of each H atom of the reference configuration. If there is a cross between two particles' indices it means that a swap of two H atoms has occurred. Here, the MC step refers to the Monte Carlo step (counted backward from the end) at which hydrogen atom exchange occurs.

we plot the permutation with the MC step that this permutation takes place, and connect each hydrogen atom through MC steps. And the last 100 hydrogen-atom permutations are shown with the step number in the figure.

The results indicate that as the MC reaches equilibrium, there is continual swapping of hydrogen atoms for both the ground state and the excited states. For the ground state a total of 16,314 permutations were recorded. For the  $168.5\text{cm}^{-1}$ ,  $2016.5\text{cm}^{-1}$  and  $3049.9\text{cm}^{-1}$  state the numbers of permutations are 2,404, 2,284 and 1,777, approximately an order of magnitude lower than that of the ground state. This indicates that although the excited states exhibit hydrogen swapping during sampling, they significantly depress the scrambling behavior of the hydrogen atoms compared to the ground state.

The low-energy and high-energy states also differ in the pattern of H atom swapping between them. At  $168.5\text{cm}^{-1}$ , exchange dynamics are dominated by four-atom permutation cycles concentrated near MC step 22662 (counted backward). In the high-energy state ( $3049.9\text{cm}^{-1}$ ), exchange events are predominantly two- or three-particle exchanges within the same observation window. The state at  $2016.5\text{cm}^{-1}$  displays a pattern similar to that of the low-energy state, suggesting it is also dominated by extensive hydrogen scrambling. Since our MC sampling began from a single arbitrary configuration, the labels assigned to the hydrogen atoms are interchangeable and have no intrinsic physical meaning.

#### IV. DISCUSSIONS

Strong anharmonicity and large-amplitude motions of hydrogen atoms in  $\text{CH}_5^+$  cause broad, diffuse bands instead of sharp, distinct peaks in its molecular spectrum. By treating large-amplitude proton motion, the NCT approach successfully captures the fluxional nature of the  $\text{CH}_5^+$ . We find that the nuclear ground state, as well as the low-lying and high-energy excited states, are highly anharmonic and exhibit similar preferences for the three stationary points on the PES. All these states undergo permutations of hydrogen atoms, as revealed by Monte Carlo sampling of their wavefunctions. In particular, the scrambling occurs more frequently for the ground state than for the excited states. Furthermore, the scrambling patterns differ across regions.

This work extends the applications of the NCT method to fluxional molecules, enabling it to solve eigenstates for systems that undergo large-amplitude spatial motion, such as  $\text{CH}_5^+$ . First, the notion of a reference configuration defined with respect to a specific equilibrium configuration cannot be applied to such molecules. This is because the PES contains a large number of equivalent minima connected by rela-

tively small energy barriers, which lead to a delocalized wavefunction. Next, using the NCT method, we present a variational approach that solves the nuclear Schrödinger equation for  $\text{CH}_5^+$ . The method scales linearly with the number of excited states. Finally, in future studies, we expect to enforce the correct hydrogen-permutation symmetry on the wavefunction to obtain more accurate energy levels. A permutation-equivariant implementation of the flow model is necessary to achieve this, as demonstrated in Ref. [65].

#### ACKNOWLEDGMENTS

We greatly thank Tucker Carrington Jr. for providing the potential energy surface of protonated methane. We are grateful for the useful discussions with Hao Xie, Xinguo Ren, Xin-Yang Dong, Lu Zhao, Zi-Hang Li, Zhen-Dong Cao, Shi-Gang Ou and Bei Qiao. This work is supported by the National Natural Science Foundation of China under Grants No. 92270107, No. T2225018, No. 12188101, No. T2121001 and the Strategic Priority Research Program of the Chinese Academy of Sciences under Grants No. XDB0500000, and the National Key Projects for Research and Development of China Grants No. 2021YFA1400400.

---

[1] P. R. Schreiner, S.-J. Kim, H. F. Schaefer, and P. Von Ragué Schleyer, *The Journal of Chemical Physics* **99**, 3716 (1993).

[2] D. Marx and M. Parrinello, *Nature* **375**, 216 (1995).

[3] D. Marx and M. Parrinello, *Science* **284**, 59 (1999).

[4] O. Asvany, P. K. P. B. Redlich, I. Hegemann, S. Schlemmer, and D. Marx, *Science* **309**, 1219 (2005).

[5] G. A. Olah, N. Hartz, G. Rasul, and G. S. Prakash, *Journal of the American Chemical Society* **117**, 1336 (1995).

[6] G. A. Olah and G. Rasul, *Accounts of chemical research* **30**, 245 (1997).

[7] E. Herbst, S. Green, P. Thaddeus, and W. Klemperer, *Astrophysical Journal* **215**, 503 (1977).

[8] D. Talbi and R. Saxon, *Astronomy and Astrophysics* (ISSN 0004-6361), vol. 261, no. 2, p. 671-676. **261**, 671 (1992).

[9] V. Tal'roze, in *Doklady Akad. Nauk SSSR*, Vol. 86 (1952) p. 909.

[10] E. T. White, J. Tang, and T. Oka, *Science* **284**, 135 (1999).

[11] O. Asvany, K. M. T. Yamada, S. Brünken, A. Potapov, and S. Schlemmer, *Science* **347**, 1346 (2015).

[12] S. Brackertz, S. Schlemmer, and O. Asvany, *Journal of Molecular Spectroscopy* **342**, 73 (2017).

[13] T. Oka, *Science* **347**, 1313 (2015).

[14] P. Bunker, B. Ostožić, and S. Yurchenko, *Journal of Molecular Structure* **695-696**, 253 (2004).

[15] A. Brown, B. J. Braams, K. Christoffel, Z. Jin, and J. M. Bowman, *The Journal of Chemical Physics* **119**, 8790 (2003).

[16] A. B. McCoy, B. J. Braams, A. Brown, X. Huang, Z. Jin, and J. M. Bowman, *The Journal of Physical Chemistry A* **108**, 4991 (2004).

[17] A. Brown, A. B. McCoy, B. J. Braams, Z. Jin, and J. M. Bowman, *The Journal of Chemical Physics* **121**, 4105 (2004).

[18] K. C. Thompson, D. L. Crittenden, and M. J. T. Jordan, *Journal of the American Chemical Society* **127**, 4954 (2005).

[19] Z. Jin, B. J. Braams, and J. M. Bowman, *The Journal of Physical Chemistry A* **110**, 1569 (2006).

[20] X. Huang, L. M. Johnson, J. M. Bowman, and A. B. McCoy, *Journal of the American Chemical Society* **128**, 3478 (2006).

[21] X. Huang, A. B. McCoy, J. M. Bowman, L. M. Johnson, C. Savage, F. Dong, and D. J. Nesbitt, *Science* **311**, 60 (2006).

[22] L. M. Johnson and A. B. McCoy, *The Journal of Physical Chemistry A* **110**, 8213 (2006).

[23] C. E. Hinkle and A. B. McCoy, *The Journal of Physical Chemistry A* **112**, 2058 (2008).

[24] C. E. Hinkle and A. B. McCoy, *The Journal of Physical Chemistry A* **113**, 4587 (2009).

[25] X.-G. Wang and T. Carrington, *The Journal of Chemical Physics* **129**, 234102 (2008).

[26] X. Wang and T. Carrington (Kos, Greece, 2015) pp. 336–337.

[27] X.-G. Wang and T. Carrington, *The Journal of Chemical Physics* **144**, 204304 (2016).

[28] C. Fábri, M. Quack, and A. G. Császár, *The Journal of Chemical Physics* **147**, 134101 (2017).

[29] R. Wodraszka and U. Manthe, *The Journal of Physical Chemistry Letters* **6**, 4229 (2015).

[30] H. Schmiedt, P. Jensen, and S. Schlemmer, *Physical Review Letters* **117**, 223002 (2016).

[31] H. Schmiedt, P. Jensen, and S. Schlemmer, *Chemical Physics Letters* **672**, 34 (2017).

[32] C. Fábri and A. G. Császár, *Physical Chemistry Chemical Physics* **20**, 16913 (2018).

[33] J. I. Rawlinson, *The Journal of Chemical Physics* **151**, 164303 (2019).

[34] J. I. Rawlinson, C. Fábri, and A. G. Császár, *Chemical Communications* **57**, 4827 (2021).

[35] I. Simkó, C. Fábri, and A. G. Császár, *Journal of Chemical Theory and Computation* **19**, 42 (2023).

[36] D. Gray and A. Robiette, *Molecular Physics* **37**, 1901 (1979).

[37] T. J. Lee, J. M. L. Martin, and P. R. Taylor, *The Journal of Chemical Physics* **102**, 254 (1995).

[38] E. B. Wilson, J. C. Decius, P. C. Cross, and B. R. Sundheim, *Journal of The Electrochemical Society* **102**, 235C (1955).

[39] S. Carter, H. M. Shnider, and J. M. Bowman, *The Journal of Chemical Physics* **110**, 8417 (1999).

[40] S. Carter and J. M. Bowman, *The Journal of Physical Chemistry A* **104**, 2355 (2000).

[41] K. Momma and F. Izumi, *Journal of Applied Crystallography* **44**, 1272 (2011).

[42] J. M. Bowman, T. Carrington, and H.-D. Meyer, *Molecular Physics* **106**, 2145 (2008).

[43] Q. Zhang, R.-S. Wang, and L. Wang, *The Journal of Chemical Physics* **161**, 024103 (2024).

[44] K. Ishii, T. Shimazaki, M. Tachikawa, and Y. Kita, *Chemical Physics Letters* **787**, 139263 (2022).

[45] Y. Saleh, Á. Fernández Corral, E. Vogt, A. Iske, J. Küpper, and A. Yachmenev, *Journal of Chemical Theory and Computation*, [acs.jctc.5c00590](https://doi.org/10.1021/acs.jctc.5c00590) (2025).

[46] R. Han, R. Ketkaew, and S. Luber, *The Journal of Physical Chemistry A* **126**, 801 (2022).

[47] S. Manzhos and T. Carrington, *Chemical Reviews* **121**, 10187 (2021).

[48] S. Manzhos, M. Ihara, and T. Carrington, in *Quantum Chemistry in the Age of Machine Learning* (Elsevier, 2023) pp. 355–390.

[49] H. Ren, H. Li, Q. Zhang, L. Liang, W. Guo, F. Huang, Y. Luo, and J. Jiang, *Fundamental Research* **1**, 488 (2021).

[50] D. Shanavas Rasheeda, A. Martín Santa Daría, B. Schröder, E. Mátyus, and J. Behler, *Physical Chemistry Chemical Physics* **24**, 29381 (2022).

[51] B. Han, R. Okabe, A. Chotrattanapituk, M. Cheng, M. Li, and Y. Cheng, *Digital Discovery* **4**, 584 (2025).

[52] R. J. DiRisio, F. Lu, and A. B. McCoy, *The Journal of Physical Chemistry A* **125**, 5849 (2021).

[53] F. Lu, L. Cheng, R. J. DiRisio, J. M. Finney, M. A. Boyer, P. Moonkaen, J. Sun, S. J. R. Lee, J. E. Deustua, T. F. Miller, and A. B. McCoy, *The Journal of Physical Chemistry A* **126**, 4013 (2022).

[54] H. X. Hao Xie, L. Z. Linfeng Zhang, and L. W. Lei Wang, *Journal of Machine Learning* **1**, 38 (2022).

[55] H. Xie, L. Zhang, and L. Wang, *SciPost Physics* **14**, 154 (2023).

[56] Z. Li, H. Xie, X. Dong, and L. Wang, *Deep variational free energy calculation of hydrogen hugoniot* (2025), [arXiv:2507.18540](https://arxiv.org/abs/2507.18540) [cond-mat.str-el].

[57] Q. Zhang, X. Wang, R. Shi, X. Ren, H. Wang, and L. Wang, *Neural Canonical Transformations for Quantum Anharmonic Solids of Lithium* (2024), version Number: 2.

[58] Q. Zhang and L. Wang, *Quantum anharmonic effects in hydrogen-bond symmetrization of high-pressure ice* (2025), [arXiv:2507.01452](https://arxiv.org/abs/2507.01452) [cond-mat.mtrl-sci].

[59] G. Papamakarios, E. Nalisnick, D. J. Rezende, S. Mohamed, and B. Lakshminarayanan, *Normalizing Flows for Probabilistic Modeling and Inference* (2021), [arXiv:1912.02762](https://arxiv.org/abs/1912.02762) [stat].

[60] I. Kobyzev, S. J. Prince, and M. A. Brubaker, *IEEE Transactions on Pattern Analysis and Machine Intelligence* **43**, 3964 (2021).

[61] R. Courant and D. Hilbert (Wiley-VCH, Weinheim, 2009) num Pages: 456.

[62] L. Dinh, J. Sohl-Dickstein, and S. Bengio, *Density estimation using Real NVP* (2017), [arXiv:1605.08803](https://arxiv.org/abs/1605.08803) [cs].

[63] F. Becca and S. Sorella, *Quantum Monte Carlo approaches for correlated systems* (Cambridge university pres, Cambridge New York, 2017).

[64] D. P. Kingma and J. Ba, *Adam: A Method for Stochastic Optimization* (2014), [arXiv:1412.6980](https://arxiv.org/abs/1412.6980) [cs].

[65] P. Wirnsberger, A. J. Ballard, G. Papamakarios, S. Abercrombie, S. Racanière, A. Pritzel, D. Jimenez Rezende, and C. Blundell, *The Journal of Chemical Physics* **153**, 144112 (2020).

### Appendix A: Supplementary Information

Table S1. The raw data of all energy levels in the 136 states calculation. The energy levels are in unit of  $\text{cm}^{-1}$ . The zero point energy is omitted here and other energy levels are reported as relative energy differences from zero point energy. Each state is measured with equivalently 100000 samples (see text for detail).

number	NCT Energy	number	NCT Energy	number	NCT Energy	number	NCT Energy
1	168.5(0.2)	35	901.5(0.5)	69	1424.5(0.4)	103	2295.2(0.3)
2	193.1(0.1)	36	901.9(0.7)	70	1433.6(0.2)	104	2305.7(0.3)
3	214.5(0.1)	37	909.8(0.4)	71	1442.6(0.2)	105	2319.5(0.4)
4	244.5(0.1)	38	933.8(0.4)	72	1488.2(0.5)	106	2321.1(0.7)
5	286.2(0.3)	39	943.1(0.4)	73	1502.3(0.5)	107	2331.0(0.9)
6	336.1(0.2)	40	1027.4(0.8)	74	1505.1(0.6)	108	2356.9(0.3)
7	383.3(0.3)	41	1036.8(0.2)	75	1506.4(1.0)	109	2364.4(0.4)
8	398.2(0.2)	42	1040.8(0.8)	76	1511.0(0.8)	110	2379.0(0.3)
9	404.0(0.4)	43	1048.8(0.4)	77	1521.3(0.6)	111	2399.7(0.6)
10	413.5(0.2)	44	1074.6(0.7)	78	1545.6(0.9)	112	2406.6(0.3)
11	421.7(0.1)	45	1129.2(0.4)	79	1564.8(0.4)	113	2470.2(0.4)
12	427.2(0.2)	46	1161.7(0.7)	80	1680.6(1.0)	114	2480.9(0.3)
13	432.6(0.2)	47	1169.3(0.7)	81	1705.6(0.6)	115	2489.4(0.3)
14	452.0(0.2)	48	1176.3(0.8)	82	1714.1(1.2)	116	2492.1(0.5)
15	466.8(0.4)	49	1188.4(0.6)	83	1715.7(0.4)	117	2507.7(0.8)
16	475.5(0.2)	50	1197.9(0.8)	84	1740.7(0.4)	118	2583.2(0.5)
17	496.3(0.4)	51	1204.2(0.4)	85	1790.1(0.6)	119	2642.2(0.4)
18	498.6(0.4)	52	1215.1(0.2)	86	1801.0(0.4)	120	2683.4(0.5)
19	566.8(0.4)	53	1244.1(0.9)	87	1828.7(0.6)	121	2810.3(0.4)
20	585.2(0.3)	54	1259.0(0.4)	88	1856.3(0.5)	122	2848.1(0.6)
21	593.7(0.3)	55	1274.4(0.7)	89	1860.4(1.7)	123	2945.5(0.8)
22	628.1(0.5)	56	1286.5(0.5)	90	1881.9(1.0)	124	3049.9(1.1)
23	646.3(0.2)	57	1296.7(0.6)	91	1890.3(0.8)	125	3062.7(1.0)
24	654.9(0.3)	58	1307.4(0.5)	92	2016.5(0.9)	126	3197.9(0.4)
25	655.1(0.4)	59	1323.2(0.7)	93	2054.1(0.2)	127	3243.4(0.2)
26	669.6(0.4)	60	1338.1(0.4)	94	2131.1(0.7)	128	3250.5(0.9)
27	725.1(0.4)	61	1353.9(0.7)	95	2172.2(1.1)	129	3285.6(0.7)
28	741.2(0.3)	62	1367.8(0.4)	96	2191.6(0.3)	130	3331.5(0.6)
29	775.8(0.5)	63	1369.0(0.7)	97	2198.7(1.0)	131	3416.5(0.4)
30	821.7(0.4)	64	1374.8(0.8)	98	2211.7(0.2)	132	3474.9(0.6)
31	830.8(0.4)	65	1380.4(1.0)	99	2223.5(0.2)	133	4160.7(0.3)
32	835.5(0.6)	66	1383.1(0.2)	100	2246.9(0.7)	134	4237.2(0.5)
33	862.0(0.4)	67	1395.8(0.4)	101	2247.2(0.9)	135	4348.8(0.7)
34	897.0(0.4)	68	1418.4(0.3)	102	2276.6(0.3)		